Ultrasonics Sonochemistry 95 (2023) 106365

Contents lists available at ScienceDirect

Ultrasonics Sonochemistry

journal homepage: www.elsevier.com/locate/ultson

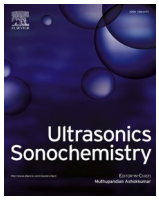

Experimental investigation on flow boiling bubble motion under ultrasonic field in vertical minichannel by using bubble tracking algorithm

Jian Xiao [a], Jinxin Zhang [b,*]

[a] School of Intelligent Manufacturing, Dongguan University of Technology-City College, Guangdong 523419, China
[b] School of Mechanical and Automotive Engineering, South China University of Technology, Guangzhou 510641, Guangdong, China

ARTICLE INFO

Keywords:
Minichannel
Ultrasonic field
Flow boiling
Bubble tracking algorithm
Motion behavior

ABSTRACT

Bubble dynamics is important in flow boiling of minichannel, and ultrasonic field effects bubble behaviors. However, flow boiling bubble movements in minichannels under ultrasonic field have received little research attention and are still poorly understood. In this paper, the effects of ultrasonic field on bubble dynamics are experimentally studied by capturing the bubble motion behaviors of the flow boiling bubbles. The ultrasonic frequencies are set to 23, 28, 32, and 40 kHz. Bubble tracking algorithm, which studies the growth, trajectories, velocities, and traveled distances for bubbles, is created to qualitatively describe bubble motion behavior of flow boiling in minichannel. It is found that after the application of ultrasound, the detachment frequency, velocity, and travel distance of the bubbles significantly increases, and the growth behavior and trajectory are extremely complex, the two-phase gas-liquid flow is extremely unstable. The bubbles gain kinetic energy as the ultrasound frequency increases. Finally, numerical simulations are used to quantitatively investigate the mechanism of bubble motion in microchannels under ultrasonic fields.

1. Introduction

Many micro-scale thermal mass transport problems must be solved as advanced engineering technologies such as microelectronic devices, biochips, and high-power LED lights are developed. The heat generation power of professional electronic devices, for example, is estimated to be greater than 1000 W/cm^2 [1,2]. Flow boiling in microchannels is highly efficient heat transfer form with enormous potential for thermal management of miniaturized electronic devices with high heat fluxes [3,4]. However, due to recent rapid increase in heat flux, microchannel flow boiling systems require corresponding improvements to improve heat transfer. Various heat transfer enhancement methods have been used to improve efficiency, compactness, and reliability of flow boiling systems.

Since the 1960s, researchers have been increasingly interested in ultrasound as a new and effective method of enhancing heat transfer [5,6]. Wong and Chon [7] conducted experiments to investigate the effects of ultrasonic vibrations on heat transfer by natural convection and boiling. They discovered that ultrasound had a significant impact on boiling heat transfer. The ultrasound effects on boiling heat transfer are being studied for the first time. The use of ultrasonic field to improve pool boiling heat transfer was demonstrated by Moehrle and Chung [8]. They discovered that ultrasonic vibrations accelerated the detachment of bubbles from a heated surface. The effect of a 40 kHz ultrasound field on pool boiling heat transfer was studied by Liu et al [9], who discovered that acoustic streaming not only increased fluid disturbance but also accelerated the formation, growth, and detachment of bubbles. The effect of ultrasonic vibrations on two-phase flow in a microchannel was investigated by Lu et al. [10]. The bubble velocity has a linear relationship with the ultrasound displacement amplitude and frequency, but the acceleration amplitude has a nonlinear relationship with frequency.

The nucleation, growth, and detachment of bubbles are caused by heat transfer generated by fluid flowing through heated wall [11,12]. As a result, the vapor mass in volume decreases, and the saturation boundary gradually expands in the fluid via conduction and convection, eventually occupying the entire channel [13]. Qin et al. [14] studied the flow field of deionized water and the growth behavior of bubbles at nucleate boiling using a high-speed camera. The visualization results showed that bubble growth is closely related to coolant flow velocity. Xu et al. [15] studied air–water mixed flow regimes in microchannel. They found that bubbly/slug flow produced bubble detachment in the immediate vicinity of the expansion nozzle, and observed the abrupt changes from annular flow to slug flow. Hoque et al. [16] used particle

* Corresponding author.
E-mail addresses: zhangjinxin@scut.edu.cn, zhangjinxin@scut.edu.cn (J. Zhang).

https://doi.org/10.1016/j.ultsonch.2023.106365
Received 15 December 2022; Received in revised form 23 February 2023; Accepted 10 March 2023
Available online 13 March 2023

image velocimetry and kinetic energy spectrum to study the effect of bubble size on kinetic energy distribution. They observed that turbulent transport and pressure diffusion term had significant contributions in the vicinity of the bubble surface. Gao et al. [17] employed high-speed imaging to investigate bubble behavior, quantificationally analyzed bubble flows generation interactions and qualitatively discussed the special conjunct bubble behavior. Studying the bubble motion during flow boiling is very important for understanding the heat transfer regimes and will contribute to various engineering systems and applications, such as the cooling of electronic components [18,19], spacecraft and aircraft thermal management [20], nuclear facilities [21],and air conditioning and refrigeration [22].

As is well known, bubble motion behavior reflects heat exchanger heat transfer efficiency. Furthermore, studying the bubble motion behavior during flow boiling can help explain the flow boiling process. Xu et al. [23] found that the fully developed turbulent gas–liquid slug flow and slug translation velocity depended on the local maximum velocity adjacent to the trailing edge of the Taylor bubbles in a long horizontal pipe with an inner diameter of 51 mm. Many methods have been employed to investigate the bubble velocity during flow boiling in minichannels [24–28]. Pavlov et al. [24] used a high-speed camera to trace the motion of a single bubble in a rectangular minichannel. They found that the velocity of the bubble in the rising direction did not follow the Poiseuille parabolic distribution and observed that wall restriction markedly disturbs the bubble wake. Kumar et al. [29] revealed that bubble velocity was closely related to the acoustic streaming, frequency, and sound intensity of the ultrasonic transducer. Kim et al. [30] experimentally investigated the bubble motion behaviors induced by acoustic streaming and found that they were a major reason for the heat transfer enhancement during pool boiling. Some researchers employed numerical simulations to investigate bubble motion behavior. Azadi [31] studied the slug bubbles motion feature in a square minichannel. The simulation results showed that the backflow region shrank with increasing liquid flow rate and bubble velocity and a significant pressure drop occurred in film flow when passing through the minimum film area. Vivekanand et al. [32] carried out numerical simulations of the effects of modulated wall motion on slug flow and heat transfer and showed that it significantly improved heat transfer. Most of those numerical simulations, which were based on their own models incorporating micro region contribution to heat transfer, have supported an important role of microlayer played to boiling heat transfer [28,33]. To study the ultrasound field effect on bubbles during flow boiling, the velocity of boiling bubble must be measured directly.

The objective of this study is to investigate bubble motion behavior of flow boiling in minichannel heat sink with and without ultrasonic field. The ultrasonic frequency is set as 23, 28, 32, and 40 kHz. Flow visualization is carried to analyze dynamic behavior of bubbles in minichannel. A new video analysis algorithm is proposed to inspect the bubble movement features with and without ultrasonic field. This exploratory study will help facilitate the application of ultrasonic fields to flow boiling in micro/micro channel heat exchangers. Our study is expected to video algorithms and inspiration for future investigations on heat transfer during flow boiling.

2. Experiment setup

2.1. Experimental system

To clear bubble behavior of flow boiling in minichannel, we design an experimental loop for the flow boiling experiments under ultrasonic field. Fig. 1 demonstrates schematic diagram of the loop, which consists of a working fluid circulation system, a visualization system, a data acquisition system and an ultrasonic field system. R141b is set as the working medium, and the physical properties are shown in Table 1. The working medium is pumped from a reservoir tank and passed through an overflow valve that spilt it into two streams. One stream return to the reservoir and the other passes through a filter to prevent clogging the flow circuit. The volumetric flow rate after injection into a thermostatic water tank is measured using a rotor flowmeter. The preheated working fluid enters the flow boiling experimental section, which is insulated with insulating wool to prevent heat loss. The working fluid is further heated and converts into a gas–liquid mixture in minichannel heat exchanger section. The working fluid is ejected from the experimental section and injected into the water chillers. After cooling, it returns to the reservoir, bringing the cycle to a close.

Table 1
Physical properties of R141b.

Boiling Point (°C)	Relative molecular mass	Specific heat ($kJ \bullet kg^{-1} \bullet K^{-1}$)	Density ($kg \bullet m^{-3}$)	Latent heat ($kJ \bullet kg^{-1}$)	Viscosity (Pa•s)
32.04	116.95	1.1636	1219.7	237.03	0.37717×10^{-3}

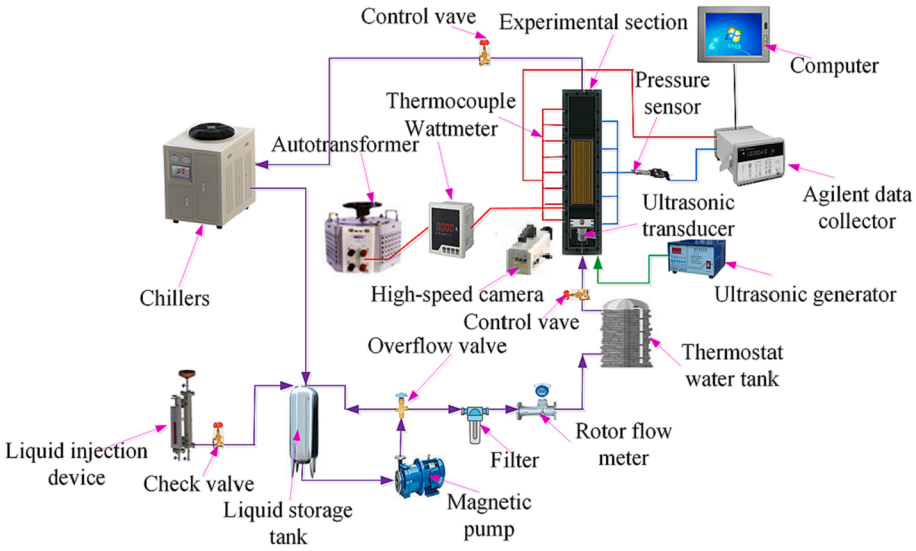

Fig. 1. Schematic diagram of experimental apparatus.

2.2. Experimental minichannel section

The minichannel section is the central component of the experimental system, and required precise manufacturing after overcoming design. A structural diagram of the minichannel section is presented in Fig. 2(a). The minichannel section comprises an aluminum alloy pedestal, rectangular minichannel heat sink, ultrasonic transducer, high borosilicate glass plate, heater plate, two sealing O-rings and cover plate. The ultrasonic transducer is installed inside the inlet, and the angle of the mounting bracket is adjusted from 0° to 90°. As shown in Fig. 2b, the heat sink had 14 rectangular minichannels with length of 220 mm, width of 2 mm in, and height of 2 mm, and their dimensons is shown in Table 2. 26 bolts hold the minichannel section together. To prevent working fluid leakage, two sealing O-rings are used. The minichannel section is covered with a 20 mm thick high borosilicate glass cover plate, which forms a rectangular heat sink and allows for flow visualization.

Fig. 3a shows the thermocouple layout on the pedestal of the minichannel heat exchanger. The upper thermocouples (T_1-T_4, T_{in} and T_{out}) are placed 5 mm below the bottom wall of the minichannel, and the lower thermocouples (T_5-T_8) are placed 19 mm below the upper thermocouples. Thermocouples (T_{in} and T_{out}) are placed 115 mm away from the sides of the minichannel and connected to the inlet and outlet buffer pools to measure the temperature of the working fluid at inlet and outlet. Thermocouples (T_1-T_4) are inserted into the measurement opening to obatin temperature of the minichannel heat sink. Thermocouples (T_5-T_8) are used to collect the temperature data from the heated part of the bottom housing. Based on those data, the effective heat flux(q_e) of the minichannel heat sink is calculated by using the following Fourier heat conduction equation:

$$q_e = -\lambda\frac{dT}{dx} = -\lambda\frac{\Delta T_{ud}}{H_w} = \lambda\frac{T_{dw} - T_{up}}{H_w} \quad (1)$$

where, ΔT_{ud} is temperature difference between the upper and lower temperature measuring points; T_{dw} and T_{up} are the lower and upper temperatures at the measurement opening; H_w is distance between the upper and lower temperature measuring points, respectively, and λ is the heat conductivity coefficient of aluminum alloy (0.155 kW/(m·K)), as shown in Fig. 3b.

The ultrasonic field is generated by a copper wire that is passed through a dedicated opening and connected to the output terminal of the ultrasound generator. As a result, the ultrasound acted directly on the working fluid, generating ultrasonic field in minichannels. In order to measure the pressure variation in the working fluid, six HC3160-HVG4 pressure sensors (P_1-P_6, shown in Fig. 4) are evenly distributed along the axial direction on the other side of the minichannel heat sink. Pressure sensors (P_1 and P_2) are arranged at the inlet and outlet, respectively, to measure the inlet and outlet pressure of the working fluid, while P_3-P_6 are evenly spaced on the side of the minichannel heat sink, measuring the pressure of the working fluid flowing through the minichannel.

Table 2
Minichannel section dimensions.

W_{ch} (mm)	H_{ch} (mm)	δ (mm)	H_w (mm)	W_w (mm)	L_{ch} (mm)
2.0	2.0	0.2	19.5	100	220

2.3. Experimental procedure

The experiments are carried out at room temperature (23.5 °C) under the following operational conditions: mass flux (G) 118.64–218.04 kg/(m^2•s), heat flux (q) 10.23–56.51 kW/m^2, inlet temperature 35.3–36.5 °C, absolute saturation pressure of minichannel section 152 ± 1 kPa, ultrasonic field frequency 23 kHz, 28 kHz, 32 kHz and 40 kHz, and sound intensity (I) 12.5 W/cm^2, 25 W/cm^2, 37.5 W/cm^2 and 50 W/cm^2. The selection for the range of ultrasonic frequencies (between 23 and 40 kHz) is due to that the acoustic flow effect and cavitation effect with enhanced heat transfer effect can be generated in low-frequency ultrasound (20 ~ 100 kHz) [6,34]. First, inert gas (N_2) is injected into the experimental system to clean the pipeline and check for any leaks. Then the system is vacuumized by a vacuum pump to remove non-condensable gases. Subsequently, the working fluid is poured into the reservoir using a filling device. Before the experiments, the working fluid is should be fully degassed by boiling in the reservoir for over than an hour to remove possible dissolved gas. The working fluid from the reservoir is then injected into the circulation loop by a magnetic pump. The working fluid is separated into two circuits using the overflow valve: the overflow working fluid in one circuit returned to the reservoir, while the fluid in the other circuit passed through a filter, rotameter, and preheated water tank, and once preheated, it entered the minichannel section where it is subjected to flow boiling. Control valves are adopted upstream and downstream in the experimental system to maintain the absolute saturation pressure in the minichannel section at about 152 kPa to ensure the constant saturation temperature of the working fluid. Next, when the mass flux and outlet pressure gradually reach the expected values, the water temperature in the thermostat tank is adjusted to

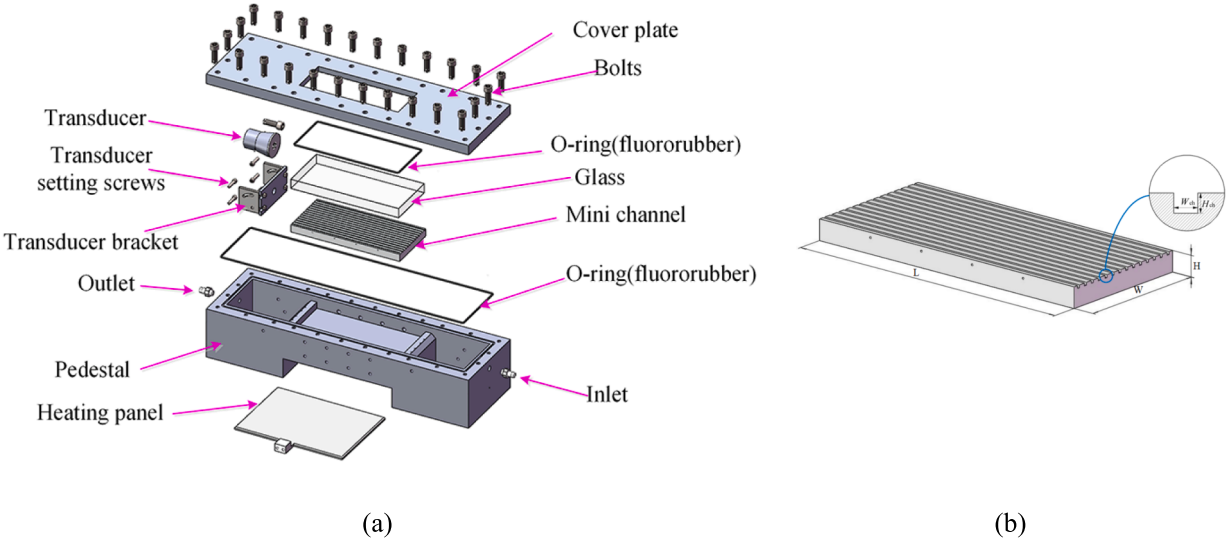

Fig. 2. Structural diagram of experimental minichannel section. (a) Experimental ultrasonic structure diagram, (b) Rectangular minichannel heat sink view.

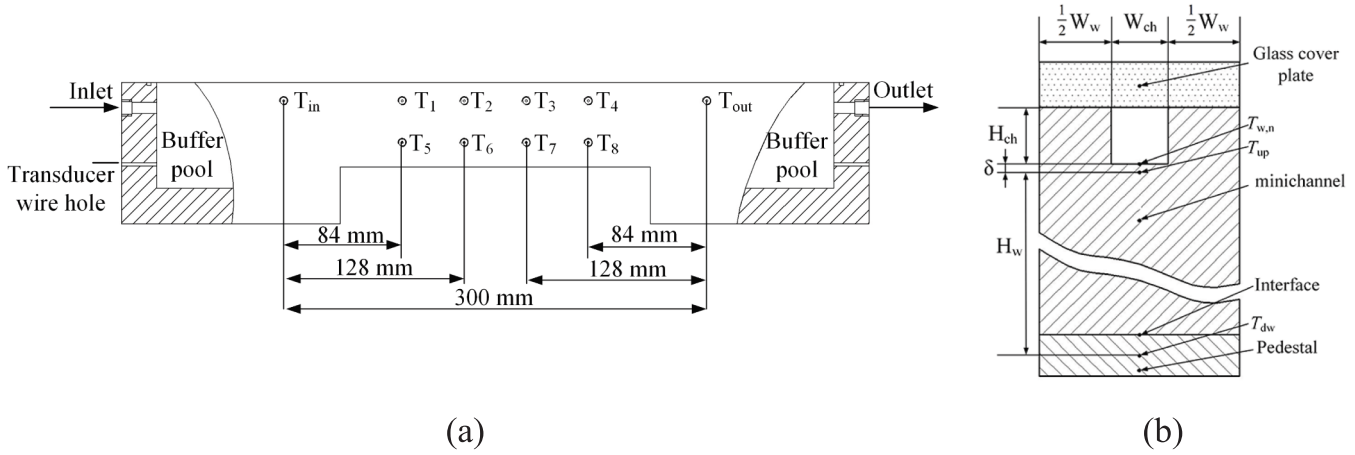

Fig. 3. Thermocouple layout in temperature measurement opening.

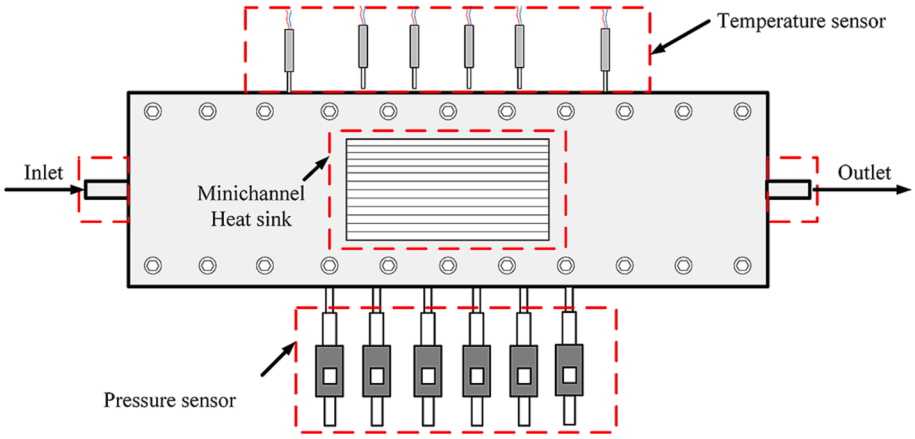

Fig. 4. Temperature and pressure sensor layouts.

achieve the required inlet temperature. Thereafter, the power supply to the heater plate is switched on and adjusted to achieve the appropriate heat flux using an autotransformer. Then, the required ultrasonic field frequency and intensity are set. An Agilent data logger is used to collect the temperature and pressure data after the system had run for 30 min to reach a steady state, while the flow boiling video image data are captured by an SVSI GigaViwe (high-speed digital camera) with a microscope of Nikon Micro-Nikkor 60 mm f/2.8D and downloaded to a personal computer for further processing. The parameters of the high-speed camera are selected as the resolution of 1280 × 128 pixels and the image capture rate of 4261 frames/s.

2.4. Flow boiling visualization

The working fluid shows significantly different two-phase flow patterns in the minichannel with or without ultrasonic field. Fig. 5 compares the two-phase flow patterns for the ultrasonic field of a frequency $f = 40$ kHz, sound intensity $I = 12.5$ W/cm^2 and radiation angle $\theta = 45°$ (It has the best enhancement ratio [35]), to those without ultrasound for different heat fluxes at the average inlet temperature $T_{in} = 35.5$ °C and $Re = 658.3$. Bubble videos in a typical portion of the heat sink are continuously acquired for the low heat flux of 10.23 kW/m^2 with ultrasonic field, as shown in Fig. 5(a). The bubbles grow and rise near the heated wall in the part bordered by red dotted box *I*, but the video is blurred due to a large number of very small bubbles present in minichannel. These bubbles are easily separated from the heated wall under ultrasonic vibrations. Consider the red-circled bubble, which gradually grows on the heated surface in frames 1–5. In frame 5, the bubble buoyancy exceeds the surface tension, and the bubble separates from the heated wall, gradually moving toward the mainstream, propelled by the combined action of fluid inertia force, buoyancy, and the ultrasonic pressure field. Because it is in the lightly overheated mainstream, the bubble had contracted by the time it appeared in frame 8. When the bubble reaches the heated wall on the other side (see frame 10), it begins to grow again gradually. The movement of this bubble reveals that the ultrasonic intervention increases the disturbance of the working fluid and chaotic convection, causing the hot fluid near the bubble to rise.

The red dotted box II in Fig. 5(a) shows that the bubble contacted intermittently and deformed more during growth due to ultrasound action. For example, in frame 1, the bubble is round, but in frame 4, it transforms into an ellipse positioned obliquely to the flow direction. In frame 8, the bubble transforms from an ellipse to a circle once more. Furthermore, the length of the bubble changes continuously during the growth process. The axial length of the bubble, for example, is 1.64 mm in frame 6, 1.86 mm in frame 10, and 1.43 mm in frame 13. These bubble deformations alter the temperature, sound, and velocity fields in the working fluid surrounding the bubbles, thereby improving the chaotic convection and promoting the mixing of cold and hot working fluids.

Fig. 5(b) shows video frames of flow boiling for a heat flux of 27.67 kW/m^2. The adjacent bubbles in the red dotted box *I* gradually merged without ultrasonic field. In the outlet area of the minichannel (red dotted box *II*), there are alternating confined and elongated bubbles, and small bubbles are entrained in the liquid film. However, in the red

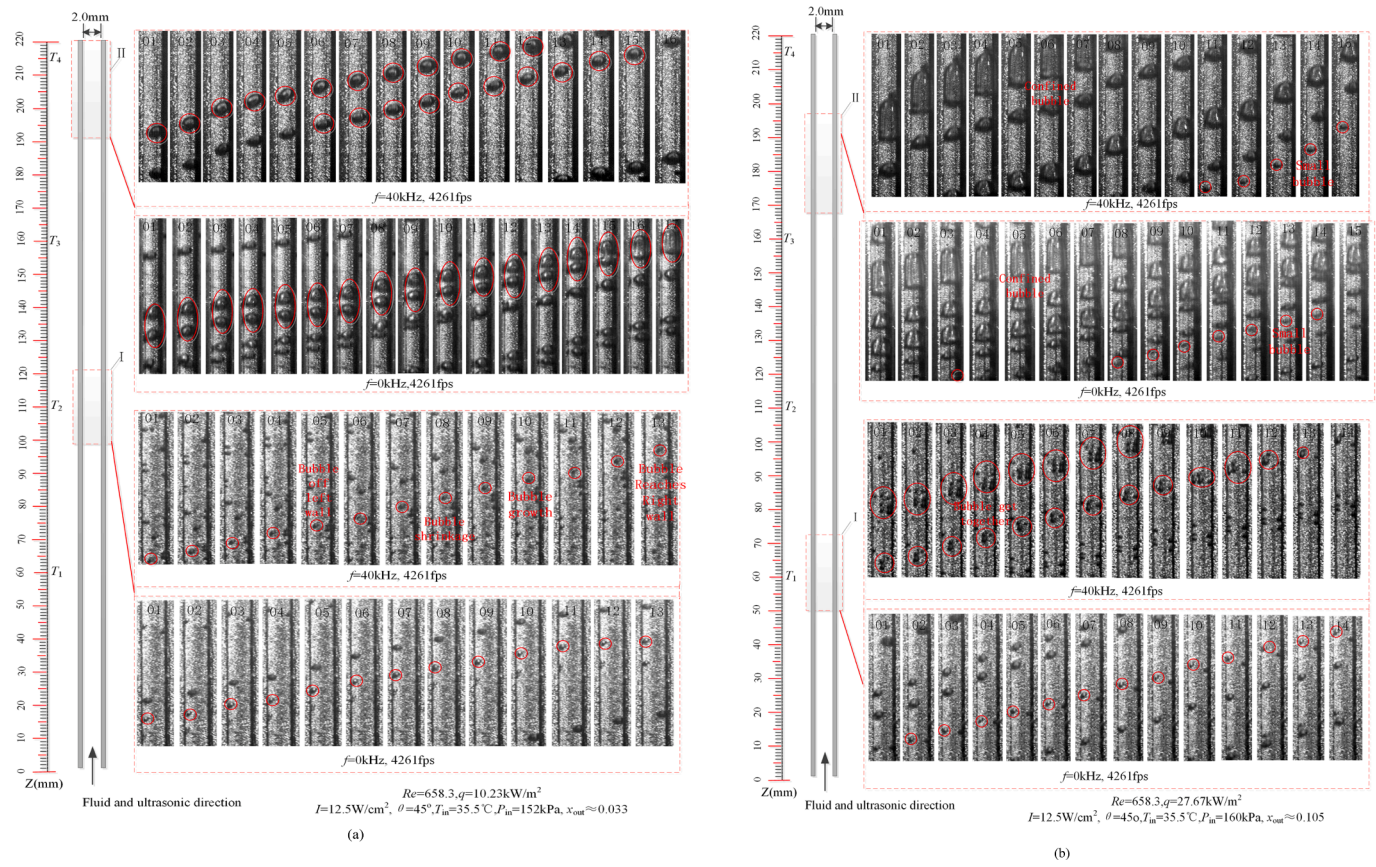

Fig. 5. Video images of minichannel representative portion with and without ultrasonic field. (a) P_{in} = 152 kPa, q = 10.23 kW/m^2 and x_{out} = 0.033, (b) P_{in} = 160 kPa, q = 27.67 kW/m^2, and x_{out} = 0.105.

dotted box *II*, due to the effect of the ultrasonic field, the minichannel is filled with a large number of small bubbles that come in intermittent contact with the heated wall. In addition, in the red dotted box *I* many bubble clusters congregate at this location, and these bubbles finally merge (as indicated by the circle), leading to the generation of new bubbles. Compared to non-ultrasonic flow boiling, the bubble transitions earlier to elongated and confined bubbles remain in this state for a long time. The specific motion features of the bubble caused by the ultrasonic field improves heat transfer.

3. Video algorithms

3.1. Video image difference image algorithm

Bubble size variation is significant for understanding the flow boiling heat transfer of the heat exchanger process. Video subtraction provides a means for quantitative analysis of bubble growth. The video algorithm is based on the inter-frame difference [36]. Bubble size variation can be revealed by subtracting the gray level between adjacent frames from the bubble. If the gray level is greater or smaller than a preselected threshold (T), then the bubble size varies and the sequence number of the video frames are record. The threshold is selected using the algorithm. Consider two adjacent frames, I_k and I_{k+1} shown in Fig. 6, whose gray level are $f(i,j,k)$ and $f(i,j,k+1)$, respectively. The gray level is defined as follows:

$$f(i,j) = \begin{cases} 1 \; if \, |f(i,j,k) - f(i,j,k+1)| > T \\ 0 \; Otherwise \end{cases} \quad (2)$$

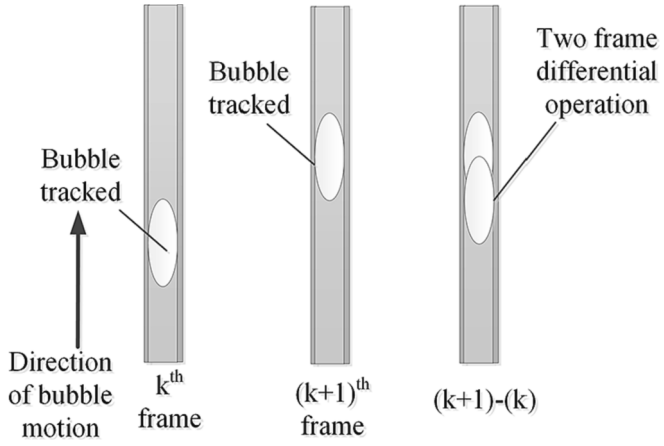

Fig. 6. The Inter-frame difference algorithm.

3.2. Video tracking algorithm

The video tracking algorithm is a new approach to investigating bubble movement trajectory. It adopts the inter-frame difference and MeanShift algorithm to locate the target [37]. The MeanShift is based on the estimation of the probability density gradient function, which is an iterative process that calculates the mean offset of the current point [38]. The point is moved to the mean value of migration and is used as a new starting point to continue moving until the iteration termination condition is satisfied. Let the traced bubble image area be denoted as, i= (1,2, …, n), where n is the number of normalized pixels. The bubble area is centered at its centroid and the weight of each point is determined by a

monotonically decreasing contour function, $k(x)$. The gray level feature of the target is described in this paper, and the weighted gray level histogram of the target is calculated, as follows:

$$p_w = C_w \sum_{i=1}^{n} k\left(\|x_i\|^2\right) \delta|b(x_i) - u| \tag{3}$$

where, u (1, 2, …, m) is the position; $\delta(x)$ is the delta function taking the values of either "1 or 0", i.e., $\delta(b(x_i)\text{-}u)$ determines whether the value of $b(x_i)$ quantized in the eigenspace of pixel x_i in the bubble area is equal to u, and $C_w = \left|\sum_{i=1}^{n} k\left(\|x_i\|^2\right)\right|^{-1}$ is the normalized constant coefficient, satisfying $\sum_{u=1}^{m} p_w = 1$. The target candidate model with y_0 as the center of the current frame is expressed as:

$$p_w(y) = C \sum_{i=1}^{n} k\left(\left\|\frac{y_0 - x_i}{h}\right\|^2\right) \delta|b(x_i) - u| \tag{4}$$

Target tracking can be simplified to the optimal y, making $p_w(y)$ most similar to q_u. Use Bhattacharyya coefficient $\rho(y)$ to measure the similarity between the target model and the candidate model, as shown in Eq. (5). The MeanShift algorithm is used to find the maximum value.

$$\widehat{\rho}(y) = \rho[p(y), q] = \sum_{u=1}^{m} \sqrt{p_w(y) q_u} \tag{5}$$

The target location process is to calculate the mean vector and update the center position of the kernel function window repeatedly according to the vector until the conditions are met. The algorithm steps are as follows:

(1) Calculate the weight of each pixel in the current windows:

$$w_i = \sum_{u=1}^{m} \sqrt{\frac{q_u}{p_w} \delta[b(x_i) - u]} \tag{6}$$

(2) Calculate the next new location of the candidate target:

$$y_1 = \frac{\sum_{i=1}^{n_h} x_i w_i \left(\left\|\frac{y_0 - x_i}{h}\right\|^2\right)}{\sum_{i=1}^{n_h} w_i g\left(\left\|\frac{y_0 - x_i}{h}\right\|^2\right)} \tag{7}$$

where $\boldsymbol{g}(\boldsymbol{x}) = -\boldsymbol{k}'(\boldsymbol{x})$

(3) If $\|y_1 - y_0\| < \varepsilon$, the calculation is stopped. Otherwise, y_1 will replace y_0 and return to the first step, and continue to search for candidate target locations that the conditions.

3.3. Video velocity measurement algorithm

Previous research has shown that increased bubble velocity and traveled distance play a significant role in improving the efficiency of heat transfer [39]. Therefore, it is necessary to study bubble velocity during flow boiling in minichannel under ultrasonic field. The video technology used in this article to measure bubble velocity has distinct desirable characteristics. It reduces costs, eliminates the need for a complicated installation process, and the system is simple, reliable, non-contact, high-precision, and has no effect on the heat exchanger. To record the steady boiling bubbles in minichannel, a photographic apparatus consisting of a high-speed digital camera, camera lens, 3-D locating device, and personal computer is set up. To capture the details of bubble movement, the high-speed digital camera shots 4,261 frames per second at a resolution of 1280 × 128. Images of a representative area of the minichannel are recorded to calculate the bubble velocity and distance traveled. A formula for calculating bubble velocity suitable for this experiment is derived. As is well known, the equation for calculating the velocity of a moving object is as follows:

$$v = \frac{\Delta d}{\Delta t} = \frac{d_2 - d_1}{t_2 - t_1} \tag{8}$$

where, v is the velocity, Δd is the distance traveled by the object, and Δt is the time interval. However, this equation cannot be used to measure the bubble velocity from video images because Δd is not directly available. According to a principle of machine vision, Eq. (8) can be rewritten as follow [40,41]:

$$v = \frac{\Delta d}{\Delta t} = \frac{d_2 - d_1}{t_2 - t_1} = \frac{f(s_2) - f(s_1)}{t_2 - t_1} \tag{9}$$

where $f(s)$ represents a monotonic function, and s_1 and s_2 are the positions of the bubble in the image, from which Δd is calculated. If two consecutive bubble images are assigned to the corresponding points, lines, or blocks, and the spatial position and angle of the high-speed camera are fixed, the pixels of the two bubbles in the video images can be mapped into one another. Let t_1 and t_2 correspond to s_1 and s_2 respectively, so that the traveled distance for the bubble in time Δt (Δt=|t_2-t_1|) is Δs (Δs=|s_2-s_1|) (shown in Fig. 7).

It can easily be seen that the unit of bubble velocity in Eq. (9) is pix/s. For the relationship between the actual velocity of the bubble and the pixel distance, Δs, the actual distance in the image, Δd, must be found. According to the principles of machine vision, a matrix relationship between s-coordinate (x, y, z) and d-coordinate (X, Y, Z) is as follows:

$$\lambda \begin{bmatrix} x \\ y \\ z \end{bmatrix} = \mathrm{A}_{3\times3} \begin{bmatrix} X \\ Y \\ Z \end{bmatrix} \tag{10}$$

Because the between-shots interval of the high-speed camera, Δt, is very small, the change in angle θ is negligible (shown in Fig. 7 (b)). In the experiment, the size (length × width) of the frame is 1280 × 128 (pix), while the minichannel width is 2 mm (shown in Fig. 7(c)). Suppose the actual displacement of a bubble in the minichannel is × (mm), then:

$$\frac{128}{2} = \frac{1280}{x\cos\theta} \tag{11}$$

In the vertical direction, the relationship between the pixel distance of the bubble image and its actual distance can be expressed by the following equation:

$$\frac{\Delta s}{1280} = \frac{\Delta d}{x} \tag{12}$$

Then, by combining Eqs. (11) and (12) following equation can be obtained:

$$\Delta d = \frac{2\Delta s}{128\cos\theta} \tag{13}$$

Thus, the actual bubble velocity in the minichannel can be obtained as follows:

$$v = \frac{\Delta d}{\Delta t} = \frac{2\Delta s}{128\Delta t\cos\theta} = \frac{\Delta s}{64\Delta t\cos\theta} \tag{14}$$

The bubble displacements between adjacent frames captured in the experiment by the high-speed camera are very small, thus θ could be ignored. To reduce the measurement error, the multi-sample and morphological erosion algorithms are used to calculate Δs. The video frame processing algorithm is as follows: (1) a Wiener filter is applied to denoise the video frame, (2) multi-sampling is used to eliminate the aliasing effect, (3) the binary and edge of the target bubble are extracted, (4) morphological erosion is performed to refine the edge definition of the target bubble, (5) the centroid of the target bubble is calculated, and (6) Euclidean distance between the current frame bubble position and the previous frame bubble position is calculated to obtain Δs. The centroid of the target bubble is calculated as follows:

$$\begin{cases} C_x = \dfrac{\sum_{i=1}^{n} C_{ix} A_i}{\sum_{i=1}^{n} A_i} \; i = 1, 2, \cdots n \\ C_y = \dfrac{\sum_{i=1}^{n} C_{iy} A_i}{\sum_{i=1}^{n} A_i} \; i = 1, 2, \cdots n \end{cases} \tag{15}$$

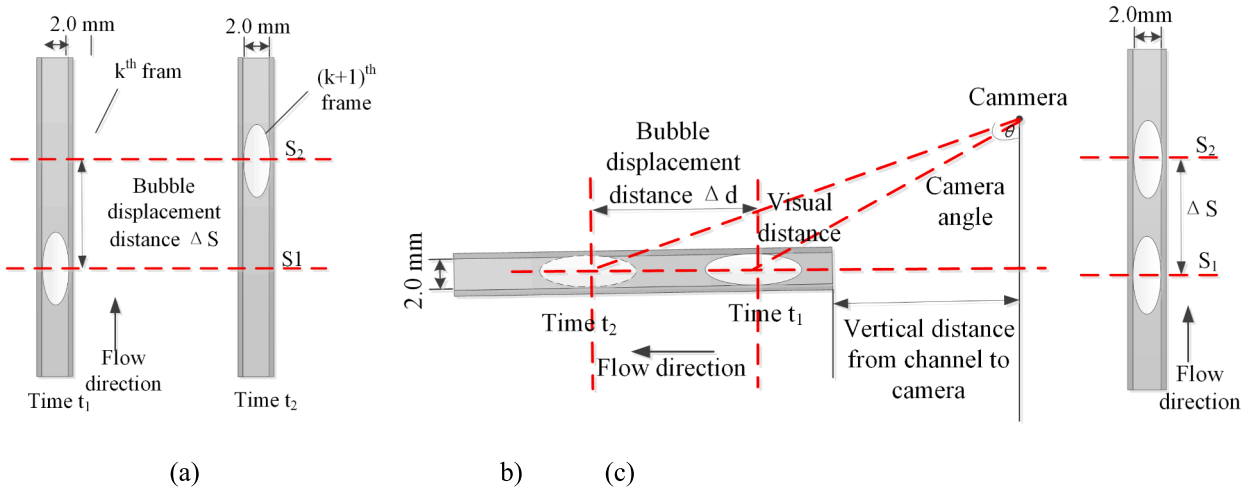

Fig. 7. Bubble velocity. (a) Front view, (b) 90° rotated view, and (c) Displacement between two-frames.

where, A_i is the triangle area inside the target bubble, and (C_x, C_y) are represents the centroid coordinates.

3.4. Algorithm verification

There are two main factors affecting the precision of image processing methods. One is the image resolution. Generally, a measurement error can occur in the small bubble size or edge of a deformed bubble [42]. Due to the instability of bubble motion, the baseline can shift by one or two pixels, especially the interface curvature. The phenomenon manifests itself as the straight-line aliasing effect, which significantly affects the measurement precision. Another factor is the effect of noise on the image [43,44]. Due to the influence of external factors, such as lighting, temperature, humidity or electromagnetic fields, the gray level distribution of image features may be degraded, resulting in errors in the bubble measurements process.

Two main methods are used to measure the velocity of bubbles based on the images, i.e., mean value and ellipsoid fit using the bubble edges [45]. The relative error, is introduced as the algorithm performance evaluation:

$$e_r = \frac{f(\bar{v}) - f(v)}{f(\bar{v})} \times 100\% \tag{16}$$

Table 3 shows the comparison between the maximum three algorithms velocity measurement errors of three algorithms applied to the same video area without ultrasound.

Table 3
Maximum relative errors of velocity measurement using different algorithms.

Bubble size /y, z /mm	Velocity range mm/ms	Average value /e_r/%	ellipse fiting /e_r/%	Video centroid /e_r/%
y < 0.5, z < 0.5	0.059 ~ 0.212	−4.7 ~ 4.2	−4.5 ~ 3.9	−4.1 ~ 4.0
0.5 ≤ y < 1, 0.5 ≤ z < 1	0.221 ~ 0.347	−3.8 ~ 4.3	−3.9 ~ 4.1	−3.7 ~ 3.9
1 ≤ y < 1.5, 1 ≤ z < 1.5	0.436 ~ 0.651	−3.2 ~ 4.2	−3.3 ~ 4.0	−3.1 ~ 3.6
1.5 ≤ y < 2, 1.5 ≤ z < 2	0.721 ~ 0.804	−2.7 ~ 3.9	−2.7 ~ 4.0	−2.6 ~ 3.6
y < 2,2 < z < 3	0.917 ~ 1.624	−2.6 ~ 3.9	−2.5 ~ 3.8	−2.2 ~ 3.2
y < 2, 3 ≤ z < 4	1.362 ~ 1.417	−2.3 ~ 4.1	−2.2 ~ 3.6	−1.9 ~ 3.0
y < 2, 4 ≤ z < 5	1.707 ~ 1.972	−1.7 ~ 3.8	−1.6 ~ 3.6	−1.6 ~ 2.8

Ref. [46] used a 5 μm needle sensor to measure the bubble velocity, and the maximum relative measurement error is about 15–20%. It can be seen that the measurement accuracy is higher than contact and achieved without the complicated debugging process or complex and cumbersome measurement equipment.

4. Results and discussion

4.1. Bubble growth

To clearly understand the influence of ultrasonic field on heat transfer, the changes in bubble size are analyzed quantitatively. Fig. 8 shows the results for the heat flux of 10.23 kW/m^2 and the ultrasonic field parameters of $I = 12.5$ W/cm^2 and $\theta = 45°$. The locations of bubble growth are all sub-cooled boiling regions and bubbles are tracked in the same region and channels with and without ultrasound field. Bubble growth is slow in the absence of ultrasonic field, and the bubble image difference in the bubble area before merging is less than 0.03 mm^2. A step increase in the tracking curve appeared after about 13–15 ms, indicating that the bubbles merge into a larger bubble. This increases the area by about 0.0483 mm^2 when compared to the original bubble. At 53 ms, the slope of the tracking curve changes. The tracked bubble has moved away from the heated surface and into the mainstream, according to the video images. The superheated degree is lower than near the heated surface, bubble growth is slower, and the working fluid is in a

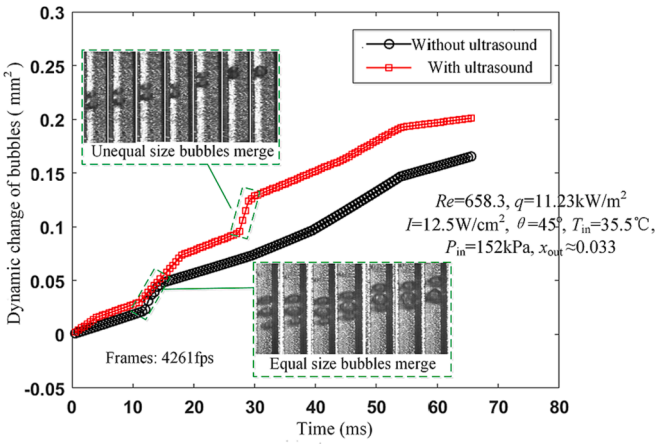

Fig. 8. Bubble growth vs. time with and without ultrasound field (Re = 658.3 and q = 10.23 kW/m^2).

sub-cooled region.

Under the action of ultrasound field, the bubble growth rate is the same as that without ultrasound field at first. However, the bubble growth curve has two points where the slope changes at 5 ms and 12 ms. It is determined from the video that the bubbles grow slowly in the mainstream from the left to the right-hand side of the heated surface. At 15 ms, the difference in the bubble area is 0.0546 mm^2. This shows that ultrasound promoted the growth of bubbles in the minichannel.

In order to quantitatively analyze the effect of ultrasonic field on bubble growth, this paper calculates the equivalent diameter of bubbles because of the irregular shape of the bubble [47].

$$D_{ed} = 2\sqrt{\frac{A_p}{\pi}} \tag{17}$$

where A_p is projected area of bubble. The edges of bubble image are extracted to calculate the equivalent diameter.

Fig. 9 show typical bubble growth process of minichannel flow boiling with and without ultrasonic field. In the free growth stage, the equivalent diameter curve of bubble with ultrasonic field is significantly smaller than without ultrasonic field, but the equivalent diameter curve with ultrasonic field is higher than without ultrasonic field in the later growth stage. This shows that ultrasound accelerates bubble growth in the later stage. In addition, we also give the change trend of bubble growth rate at different stages. It can be also seen that, the bubble growth rate with ultrasonic field is always greater than without ultrasonic field in the later growth stage. In general, the growth rate of the bubble with ultrasonic field is higher than that without ultrasound field.

In Fig. 8, without ultrasonic field, in the sub-cooled boiling region, the bubble growth mainly occurs through the merging of adjacent bubbles and the evaporation on the bubble surface. In the boiling region, most of the working fluid do not reach the saturation temperature and the temperature of the heated surface is higher in the channels, thus the superheated degree is high. The tracked bubbles grow rapidly into large bubbles by merging with adjacent bubbles or by evaporation. The action of ultrasound results in a drop in the heated surface temperature and superheated degree. In addition, the liquid is partially subcooled, thus the evaporation capacity decreased and the bubble growth is slow. In the sub-cooled boiling region, the temperature of the working fluid is boiling. In the absence of the ultrasonic field, the working fluid has a high superheated degree and evaporation capacity is strong. The bubbles grow on the heated surface, resulting in a decrease in vapor volume and slow bubble growth. In this state, the bubble growth depends on merging with other bubbles to form a bigger bubble. However, under the ultrasonic field, the cold working fluid is continuously transported to the vicinity of the heated surface, resulting in a drop in the heated surface temperature and superheated degree. Although the working fluid is boiling, the heated surface below the superheated point still causes the oncoming cold working fluid to evaporate. This accelerates the growth of the bubble. It is hypothesized that bubble merging did not occur during the growth process, and that the bubble growth rate under ultrasonic field is greater than that under non-ultrasound. If bubble merging is taken into account, the bubble growth rate without ultrasonic field may be faster than that with ultrasonic field, because merging into large bubbles is easier without ultrasound field.

4.2. Bubble kinematic velocity and traveled distance

Bubble dynamic such as bubble growth, detachment, and sliding can be attributed to the improved flow boiling heat transfer. The sliding of the bubbles disturbs the thermal and velocity boundary layers, increasing heat transfer between the refrigerant and the heated wall [48,49]. The video images show that the ultrasonic field significantly alters the sliding trajectories of bubbles. As a result, more research into the ultrasonic field effects on the velocity and traveled distance by sliding in flow boiling is required. Fig. 10 shows the bubble motion behaviors with or without ultrasonic field in the low thermodynamic equilibrium quality area with $q = 10.23$ kW/m^2, $Re = 658.3$, and $\Delta T_{sub} = 8$ °C. Without ultrasonic field (see Fig. 10(a)), the bubble remains relatively close to the unilateral wall. This type of bubble sliding causes little disturbance to the working fluid, and cannot move cold working fluid to the heated wall. Agostini et al. [50] also observed this phenomenon when studying the influence of bubble velocity on heat transfer. However, under the action of ultrasonic field with $f = 40$ kHz, $I = 12.5$ W/cm^2, and $\theta = 45°$, the bubble along a channel slide moves forward and oscillated between the left- and right-hand side heated walls, as shown in Fig. 10(b). On one hand, this type of bubble sliding is clearly beneficial to transferring cold working fluid to the heated wall, and promoting the mixing of hot working fluid near the heated wall and cold working fluid in the mainstream both of which are conducive to improving flow boiling heat transfer [51].

The integrity of the downstream superheated working fluid layer is

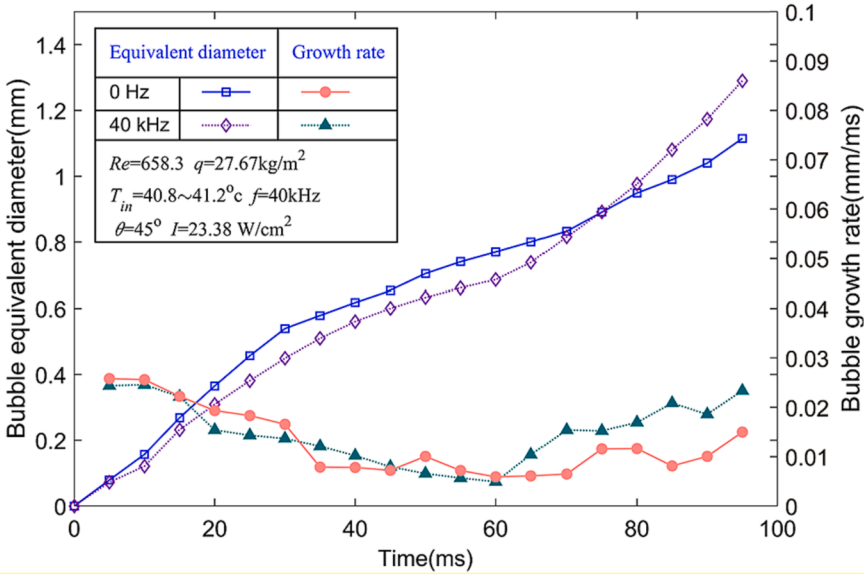

Fig. 9. Typical bubble growth process of minichannel flow boiling with and without ultrasonic field.

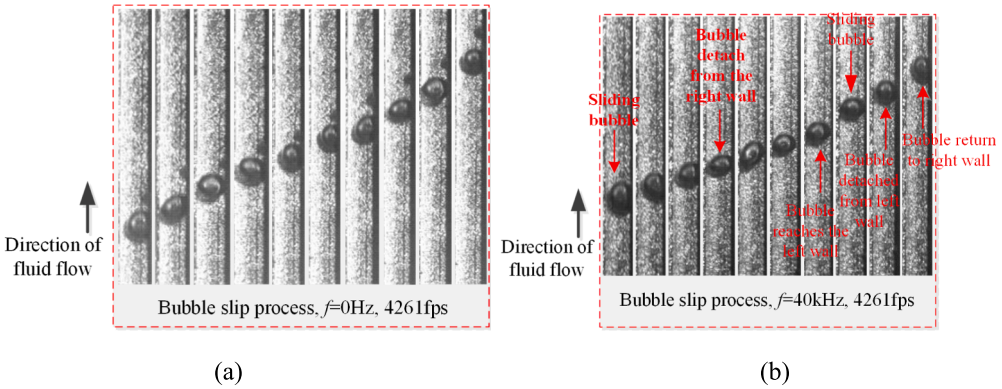

Fig. 10. Bubble motion (q = 10.23 kW/m^2, Re = 658.3, and ΔT_{sub} = 8 °C). (a) f = 0 kHz, (b) f = 40 kHz.

destroyed during sliding along flow direction, allowing the subcooled working fluid to supplement the effective evaporation area at the bubble root. Because evaporation at the bubble root interface is weakened, bubble size changes slowly during sliding. It has moved away from the heated wall and toward the mainstream during sliding. For transient heat conduction, the working fluid is supplemented to the superheated wall. This phenomenon can enhance flow boiling heat transfer in microchannels, which has been confirmed by Refs. [52,53]. The preceding discussion indicates that bubble motion had a significant impact on heat transfer, and the velocity and traveled distance directly indicated the bubble motion state. Fig. 11 shows how bubble velocity and traveled distance varied with time under the conditions of q = 10.23 kW/m^2 and Re = 658.3, ultrasound parameters of I = 12.5 W/cm^2 and θ = 45°, and the frequencies of 0 Hz, 23, 28, 32, and 40 kHz. It can be seen that the bubble velocity is markedly different in the early and late stages of the movement. Thus, the movement can be divided into two stages: low-velocity and high-velocity movement. During the low-velocity stage, the bubbles moved slowly upward along the heated wall because small bubbles gained little lift. The bubble velocity and traveled distance are very small with or without ultrasonic field. However, during the high-velocity stage, the bubbles gain greater momentum under the action of ultrasonic field and move faster and farther. The velocity and traveled distance plot become steeper with the increase in ultrasonic frequency and the energy obtained by the bubble increases with the increase in frequency. Moreover, it is also observed in the video images that in the low-velocity sliding stage, the bubble diameter increases slowly and the bubble contact angle changes little. However, in the high-velocity stage, the bubble diameter and contact angle begin to decrease slowly. This happens because when the bubble enters the high-velocity sliding, it breaks away from the heated wall and moved toward the mainstream. The bubble root is in the superheated working fluid layer. By now, the gas–liquid interface gradually decreases, and more bubble interfaces contact with the subcooled mainstream working fluid, resulting in weakened evaporation on the bubble interfaces and enhanced condensation. The bubble size decreases gradually after it enters the high-velocity sliding stage. When the bubble sliding velocity reaches a certain value, the bubble completely separates from the wall and becomes the bubbly flow.

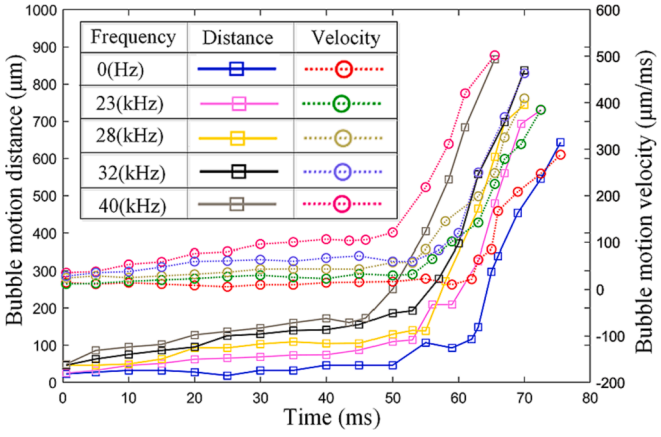

Fig. 11. Bubble velocity and distance vs. time with and without ultrasonic field.

In order to clearly visualize the bubble trajectories, a new coordinate system is introduced. The left-hand side wall inside the minichannel is taken as the z-axis, the width as the y-axis and the left-hand side wall at the inlet as the coordinate system origin. When the bubble enters the region of view, the first frame image is captured by the high-speed camera, the distance from the bubble to the left-hand side wall is calculated and this position is marked with an "O". Fig. 12 illustrates the bubble trajectory under the conditions of q = 10.23 kW/m^2 and Re = 658.3. With no ultrasonic field (see Fig. 12(a)), the bubble enters the region of view from the right, and slid and rose slowly along the heated wall. The bubble merges with other bubbles twice during its ascent, resulting in the bubble sliding towards the left-hand side wall. The entire bubble trajectory is essentially stable while sliding along a straight line on the wall. However, when ultrasonic field is applied (see Fig. 12(b)), the bubble oscillates back and forth between the walls while moving upward. Furthermore, sometimes the bubble jumpesd and is found in a very unstable state. On the one hand, this type of movements is helpful to transfer cold working fluid to the heated wall. On the other hand, it stirs the mixing of hot working fluid near the heated wall and cold working fluid in the mainstream. The high-speed camera recordes 133 frames without ultrasonic field and 117 frames with ultrasonic field of a single bubble moving through the region of view over the same time and at the same location. This means that the rising speed of the bubble is faster when the ultrasonic field is applied, or that the buoyancy of the bubble with ultrasonic field is greater than that without ultrasonic field.

4.3. *Influence on bubble motion*

The direct reason for the change in bubble velocity is the instability of two-phase flow caused by the confined bubble growth and elongation. Different heat flux or mass flux conditions has an important effect on bubble confinement and elongation; thus, they also strongly influence the instability of flow boiling. The boiling number is usually used to characterize the combined effect of heat flux and mass flux on flow boiling instability [54]. The larger the boiling number, the stronger the instability of flow boiling in minichannel. Therefore, the study of the influence of operating conditions on bubble motion will consider the boiling number, Bo, which is defined, as follows:

$$Bo = \frac{q}{Gh_{fg}} = \frac{qv}{\lambda \rho_g} \tag{18}$$

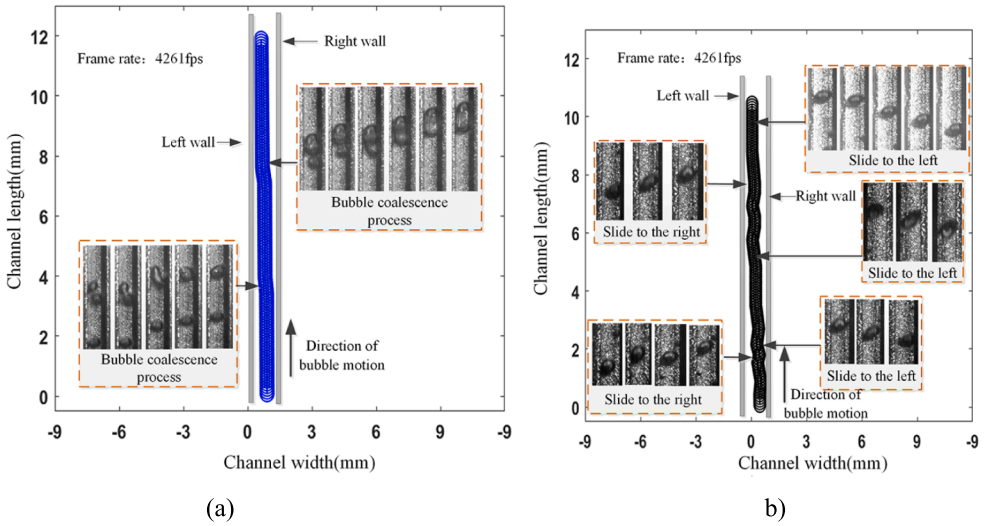

Fig. 12. Bubble trajectories with and without ultrasonic field. (a) $f = 0$ kHz, (b) $f = 40$ kHz.

here h_{fg} denotes latent gasification heat, and v represents the fluid velocity in the boundary layer.

Fig. 13 shows the influence of changing the boiling number on bubble velocity and traveled distance with and without ultrasonic field. It can be seen in the figures that in the low-velocity stage, whether there is ultrasonic field or not, the bubble velocity and traveled distance at different boiling numbers are very close and very small. The velocity loges at the end of the movement along the heated wall (i.e., the moment when the bubble separates from the heated wall). Then, the particle moves along the flow direction, which increases with the increase in boiling number. In the absence of ultrasonic field, the boiling number strongly affects the constrained growth and elongation of bubbles in the moderate thermodynamic dryness region. The larger the boiling number, the faster the growth rate of confined or elongated bubbles, and the shorter the time requires to develop into confined or elongated bubbles. As a result, the instability of gas–liquid two-phase flow become severer, the bubbles gains more kinetic energy, the sliding distance is longer, and the bubbles separates from the heated wall at a faster velocity. This is essentially consistent with the experimental observations found in Ref. [55]. With the application of ultrasonic field, in the high-velocity stage, the traveled distance for bubbles and their velocity are markedly higher than without the ultrasonic field. By comparing the bubble's traveled distance and velocity curves with and without ultrasonic field, it is found that the time of bubble sliding along the heated wall with ultrasonic field is shorter than that without ultrasonic field, and it takes less time for confined or elongated bubbles to grow at the same boiling number. The gas–liquid two-phase flow is very unstable, and the bubble has greater kinetic energy, a longer traveled distance, and detaches from the heated wall at a higher velocity. This shows that the ultrasonic field fluctuations promote heat transfer.

4.4. Error analysis

This paper attempts to improve the bubble velocity and distance measurement accuracy by image algorithm. The relative measurement error of the bubble velocity and distance, which is expressed by Eq. (16). Fig. 14 show relative error of measured velocity and distance under 0 Hz, 23 kHz, 28 kHz, 32 kHz, and 40 kHz. The measurement error is divided into two parts: low-velocity motion and high-velocity motion. The results imply that most of the relative measurement error are within ± 4%. Relative to the ultrasonic field condition, the relative error of the non-ultrasonic field is less than 1% in the low-velocity region and 2% in high-velocity region. The analysis of the video image shows that the high-velocity motion of bubbles leads to the blur of the image. In addition, the ultrasonic filed vibration also causes the blur of the image, and this phenomenon becomes more apparent as the frequency of the ultrasonic field approaches that of the camera. The filtering algorithm to eliminate the blur of bubble image under high-velocity motion needs

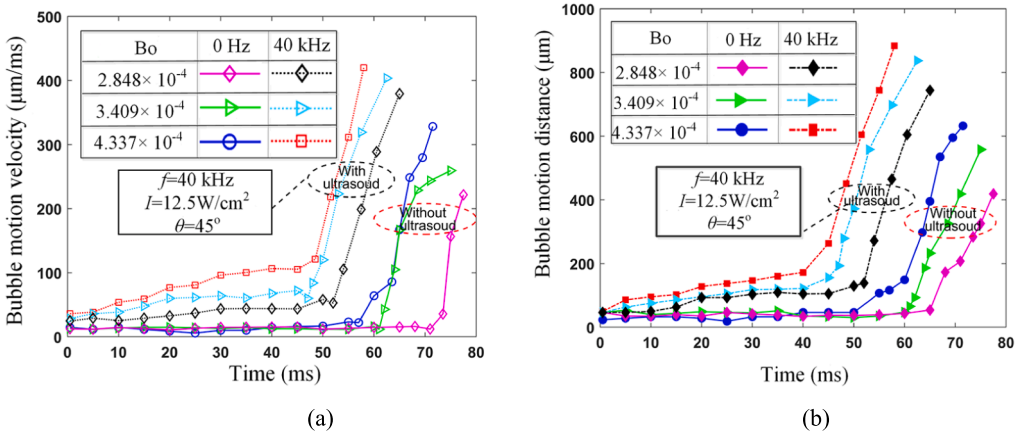

Fig. 13. Bubble movements with and without ultrasonic field. (a) Bubble velocities, (b) Traveled distances.

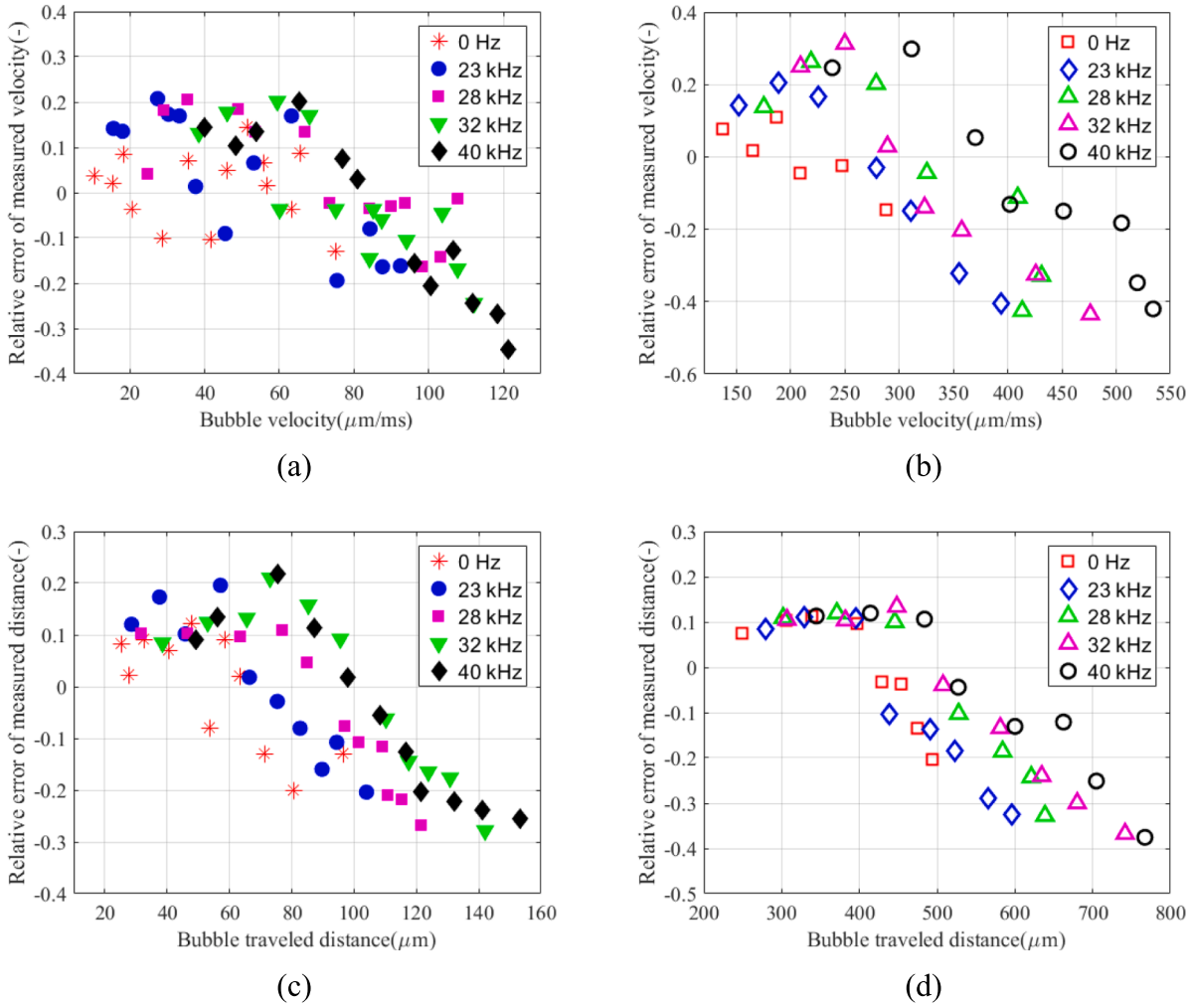

Fig. 14. Relative error of measured velocity and distance. (a) Velocity relative error low-velocity, (b) Velocity relative error High-velocity, (c) Traveled distance relative error low-velocity, (d) Traveled distance relative error high-velocity.

further research.

4.5. Bubble kinetics analysis

The video analysis results show that the bubble motion behaviors with ultrasonic field are significantly different from those without ultrasonic field. The bubble motion features are closely related to the various forces acting on the bubbles in the channel. Therefore, bubble kinetic analysis can be used to understand the mechanism of bubble motion behaviors under ultrasonic field. Those are divided into two categories: one is from the bubble itself, and the other is applied by the outfield (such as ultrasonic, electric field, etc.) [56]. This paper adopts MATLAB numerical simulation code to analyze the forces acting on a bubble.

As shown in Fig. 15a, the width, height and length of the calculation domain for single minichannel are 2 mm, 2 mm and 10 mm respectively. The ultrasonic field is a sinusoidal wave. The acoustic pressure is transmitted in the *y* and *z* directions, and its frequency is 40 kHz and the acoustic intensity12.5 W/cm^2. The Poisson's ratio is 0.5. The minichanels satisfies the Dirichlet condition and the bubble arc satisfied the Neumann condition. The optimization grid is displayed in Fig. 15 (b). Grid deformation technology is utilized in numerical simulations.

The ultrasonic pressure field exerted on a bubble act in *yz*-plane, *x*-axis free, and R141b is the same nature and homogenous. Therefore, the stress–strain relationship is as follows:

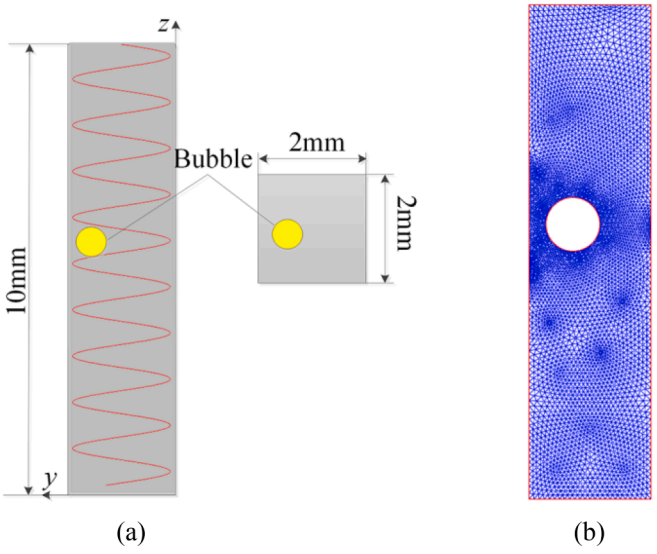

Fig. 15. Computational domain and grid with bubble. (a) Computational domain. (b) Grid.

$$\begin{pmatrix}\sigma_z\\ \sigma_y\\ \tau_{yz}\end{pmatrix}=\frac{E}{1-p^2}\begin{pmatrix}1 & p & 0\\ p & 1 & 0\\ 0 & 0 & \frac{1-p}{2}\end{pmatrix}\begin{pmatrix}\varepsilon_z\\ \varepsilon_y\\ \gamma_{yz}\end{pmatrix} \tag{19}$$

where, σ_y and σ_z are stresses along y and z directions, respectively, τ_{yz} is the shear, E is Young's modulus, and p Poisson's ratio. Bubble displacement in y and z directions are denoted by $\boldsymbol{u}$ and $\boldsymbol{v}$, respectively, and the following relations hold for the strain:

$$\varepsilon_z=\frac{\partial u}{\partial z},\ \varepsilon_y=\frac{\partial v}{\partial y},\gamma_{yz}=\frac{\partial u}{\partial z}+\frac{\partial v}{\partial y} \tag{20}$$

Force balance equations are as follows:

$$\begin{cases}-\frac{\partial\sigma_z}{\partial z}-\frac{\partial\tau_{yz}}{\partial y}=K_z\\ -\frac{\partial\tau_{yz}}{\partial z}-\frac{\partial\sigma_y}{\partial y}=K_y\end{cases} \tag{21}$$

where K_z and K_y are acoustic pressure. Equation (19) can be normalized to obtain the following system of elliptic equations:

$$-\nabla\cdot(c\otimes\nabla u)=K \tag{22}$$

where, $\boldsymbol{u}$ is a 2-D vector, and c is the following tensor of rank 4 and 2×2 matrix:

$$\begin{aligned}c_{11}&=\begin{pmatrix}2S+\mu & 0\\ 0 & 0\end{pmatrix}c_{12}=\begin{pmatrix}0 & \mu\\ S & 0\end{pmatrix}\\ c_{21}&=\begin{pmatrix}0 & S\\ \mu & 0\end{pmatrix}c_{22}=\begin{pmatrix}S & 0\\ 0 & 2S+\mu\end{pmatrix}\end{aligned} \tag{23}$$

where S denotes shear modulus, and the definition $S=\frac{E}{2(1+v)}$ $\mu=2S\frac{v}{1-v}$, and $K=\begin{pmatrix}K_z\\ K_y\end{pmatrix}$

The force at the gas–liquid interface is as follows:

$$F_v=\sqrt{2I\rho c}\sin(2\pi ft) \tag{24}$$

where I represent acoustic intensity, ρ is the medium density and c is the acoustic velocity. These physical parameters are provided in Table 4.

Bubbles motion behaviors in the minichannel are governed by forces. When a bubble is attached to the heated wall and does not move, all forces must be balanced, i.e.:

$$\sum F_z=F_{sz}+F_{bgz}+F_v+F_{qsz} \tag{25}$$

where, F_{sz} is the surface tension, F_{bgz} is the bubble growth force, F_{qsz} is the drag force, and F_v is the acoustic pressure.

The following assumptions are made in the simulation model:

(1) Bubble attached to the heated wall is spherical when surface tension acted, thus its 2-D model is circular.
(2) Only the acoustic pressure and drag forces are considered, and all other forces are ignored.
(3) Bubble is assumed rigid, i.e., Young's modulus is 1.
(4) Bubble do not grow during movement.

Table 4
Physical parameters of the media.

Materials	Density /kg/m^3	Acoustic velocity /m/s
Aluminum alloy	2830	6400
R141b liquid- phase	1196.3	750.4
R141b gas- phase	7.1	151.1

Fig. 16 shows the forces acting on the bubble while it is simulated numerically to move from the left toward the right wall. Acoustic pressure distributed changes near bubble by bubble existing in the figure. When the bubble is near the left heated wall, F_v is weakened near the wall gas–liquid interface of the bubble. However, it is intensified on the other side. The drag force, F_{qsz}, that prevented the bubble from moving upward is much larger than on the other side. The numerical simulation reflects the bubble movement trend toward the middle of the channel of the heated wall at an angle. While the bubble is in the middle of the channel, the numerical simulation reveals that the two sides of the bubble interface are approximately equal to F_v and F_{qsz}. The bubble moves upward the flow direction. The behavior of the bubble movement is influenced by the fluctuation of ultrasonic field. This issue essentially consistent with observations made from the high-speed camera images.

In the absence of ultrasonic field, the bubble slides on the heated wall along the flow direction. The confined and elongated bubble forms a pressure peak in the fluid near the bubble, which has an effect similar to a throttle valve [57]. The gas–liquid two-phase working fluid flow is unstable, which violates the force balance of the bubble attached to the heated wall in the upstream area for low thermal mechanical dryness along the flow direction. This fact causes bubbles to move in a sliding manner near the heated wall. At the initial stage of sliding, the bubble growth rate hardly changes. At this time, the growth force along the flow direction could be ignored, and the force components that affects the sliding motion behavior of bubbles in the flow direction includes only surface tension and drag force. The surface tension of the bubble interface could be adjusted by the contact angle for keeping the mechanical balance. The bubbles slide along the heated wall when the dynamic balance relationship is violated. During the bubble sliding process, this delicate balance is still kept by the surface tension and drag force. As bubbles continues to grow and elongate or merge with other bubbles to form elongated confined bubbles in downstream, this leads to the pressure peak, suddenly disappearing and causing severe two-phase gas–liquid two-phase flow instability. The surface tension and drag force balance are irreversible destroyed, thus working fluid flow velocity increases significantly in downstream. As the bubble accelerates, it enters a high-speed sliding state, departs from the heated wall and joins the mainstream. In a word, the forces that acted on the bubble during flow are out of balance, resulting in the bubble sliding movement in the low thermal dryness area of flow boiling. While in the proper thermodynamic dryness region, the kinetic balance is violated by the bubble confined growth, merger and elongation behavior, which lead to flow instability.

Under the action of ultrasonic field, the resultant force of ultrasonic field pressure is generated in the y and z directions, so that the above balance forces are violated earlier and bubbles moved between walls. The surface tension and drag force that acted on the bubble are weakened by ultrasonic field cavitation and oscillation [58], thus bubble velocity increases and bubble merging into elongated confined bubbles is faster. The ultrasonic field makes the contact angle between the bubble and the wall smaller, which intensifies the instability of the gas–liquid two-phase working fluid.

5. Conclusions

This study focuses on investigating flow boiling bubbles motion behavior in a vertical minichannel heat sink in the presence of ultrasonic field. An ultrasonic transducer is placed inside the heat sink inlet with the mounting angle from 0° to 90°. Several video algorithms are introduced to quantitatively analyze flow boiling bubble movement features with and without ultrasonic field. The main findings are as follows:

(1) For the experimental conditions of heat flux 10.23 kW/m^2 or 27.67 kW/m^2 and Reynolds of 658.3, ultrasonic field produces more and smaller bubbles, which leads to video images blurring in the same parts of the flow in the minichannel compared to the

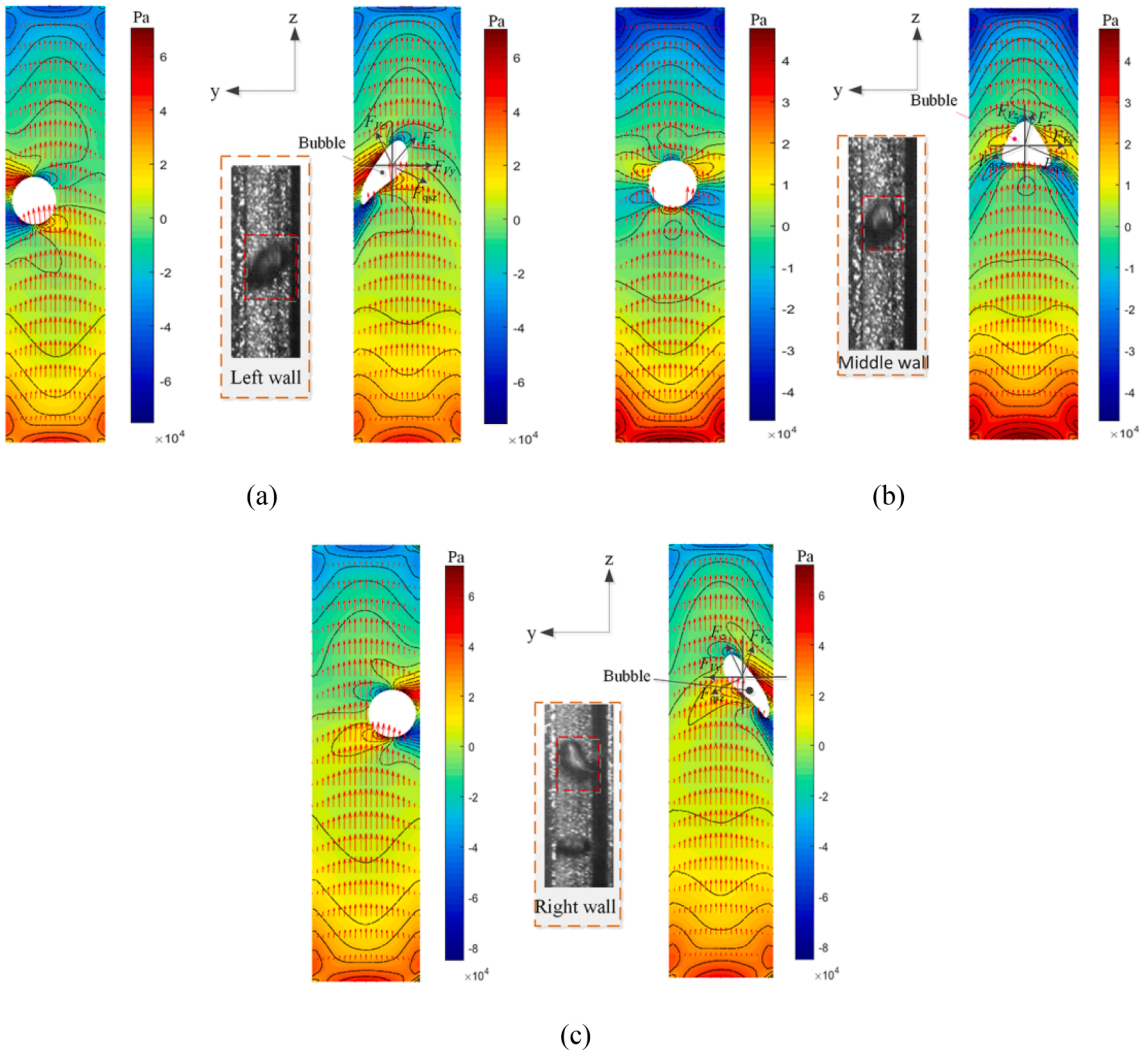

Fig. 16. Ultrasonic field pressure distribution at bubble different positions. (a) Left wall, (b) Middle wall, and (c) Right wall.

same flow without ultrasonic field. It is also observed that in higher frequency ultrasonic field bubble clusters forms more easily. Furthermore, ultrasonic field enhances the mixing of hot and cold working fluid and reduces the axial length of bubbles. Increased bubble production with ultrasonic field leads to an earlier transition from bubbly flow to slug flow and an earlier transition from slug flow to churn or annular flow.

(2) In the bubble flow under the same conditions, the video tracking algorithm found that the bubble area difference is 0.0546 mm^2 with ultrasonic field, while it is 0.0483 mm^2 without ultrasonic field. At higher frequencies, bubble morphology is more likely to change during bubble growth. The video trajectory algorithm reveals that the bubble oscillates between the walls in an S-shaped movement and instability increases with the frequency. This is beneficial for cold working fluid to contact with the heated wall. The video image velocity determination algorithm reveals that the bubble motion develops in two stages: a low-speed phase and a high-speed phase, the bubble velocities and distances with time are similar with and without ultrasonic field in the low-speed phase. In the high-speed phase, those are significantly faster and further, and these trends become more pronounced as the ultrasonic field frequency increases.

(3) A pressure simulation model and grid deformed technology are utilized to analyze bubble forces numerically. The existence of bubble causes a pressure spike to form in the fluid near the bubble and produced gas–liquid two-phase working fluid instability. The ultrasonic field reduces surface tension and drag forces acting on the bubble, making the contact angle between the bubble and heated wall smaller, aggravating instability of flow boiling and complicating bubble motion behavior. The bubble deformations observed in the simulation are very close to video images.

CRediT authorship contribution statement

Jian Xiao: Conceptualization, Visualization, Methodology, Formal analysis, Writing – original draft, Writing – review & editing. **Jinxin Zhang:** Funding acquisition, Project administration, Supervision, Writing – review & editing.

Declaration of Competing Interest

The authors declare that they have no known competing financial interests or personal relationships that could have appeared to influence the work reported in this paper.

Acknowledgments

The authors acknowledge the financial support provided by both the Major Projects of Guangdong Education Department for Foundation Research and Applied Research (No. 2021KTSCX189), The Science and

Technology Bureau R&D Project of Dongguan (No. 20211800500052), and the Major Scientific Research Projects of Dongguan City College (No. 2021YZDYB05Z).

Data availability

The data that support the findings of this study are available from the corresponding author upon reasonable request.

References

[1] J. Lee, I. Mudawar, Low-temperature two-phase microchannel cooling for high-heat-flux thermal management of defense electronics, IEEE Trans. Comp. Packag. Technol. 32 (2009) 453–465.
[2] G. Liang, I. Mudawar, Review of single-phase and two-phase nanofluid heat transfer in macro-channels and micro-channels, Int. J. Heat Mass Transfer 136 (2019) 324–354.
[3] N. Mao, J. Zhuang, T. He, M. Song, A critical review on measures to suppress flow boiling instabilities in microchannels, Heat Mass Transfer. 57 (2021) 889–910.
[4] D. Deng, L. Zeng, W. Sun, A review on flow boiling enhancement and fabrication of enhanced microchannels of microchannel heat sinks, Int. J. Heat Mass Transfer 175 (2021), 121332.
[5] H. Daghooghi-Mobarakeh, M. Daghooghi, M. Miner, L. Wang, R. Wang, P. E. Phelan, Augmentation of natural convection heat transfer in enclosures via ultrasound: Effects of power, frequency and temperature, Therm. Sci. Eng. Progr. 33 (2022).
[6] M. Dehbani, M. Rahimi, Z. Rahimi, A review on convective heat transfer enhancement using ultrasound, Appl. Therm. Eng. 208 (2022) 118273.
[7] S.W. Wong, W.Y. Chon, Effects of ultrasonic vibrations on heat transfer to liquids by natural convection and by boiling, AIChE J. 15 (1969) 281–288.
[8] R.E. Moehrle, J.N. Chung, Pool boiling heat transfer driven by an acoustic standing wave in terrestrial gravity and microgravity, Int. J. Heat Mass Transfer 93 (2016) 322–336.
[9] F.-C. Liu, S.-W. Chen, J.-D. Lee, Feasibility study of heat transfer enhancement by ultrasonic vibration under subcooled pool condition, Heat Transfer Eng. 39 (2017) 654–662.
[10] Z. Lu, E.D. Dupuis, V.K. Patel, A.M. Momen, S. Shahab, Ultrasonic oscillatory two-phase flow in microchannels, Phys Fluids 33 (3) (2021) 032003.
[11] X. Yin, C. Hu, M. Bai, J. Lv, An investigation on the heat transfer characteristics of nanofluids in flow boiling by molecular dynamics simulations, Int. J. Heat Mass Transfer 162 (2020) 120338.
[12] S. Azizifar, M. Ameri, I. Behroyan, Subcooled flow boiling of water in a metal-foam tube: An experimental study, Int. Commun. Heat Mass Transfer 118 (2020).
[13] Z. Rui, F. Zhao, H. Sun, L.i. Sun, H. Peng, Experimental research on flow boiling thermal-hydraulic characteristics in novel microchannels, Exp. Therm. Fluid Sci. 140 (2023) 110755.
[14] L. Qin, X. Zhang, J. Hua, X. Zhao, S. Li, Flow boiling performance and bubble behaviors of non-closed droplet micro pin-fin arrays, Int. Commun. Heat Mass Transfer 133 (2022) 105918.
[15] H. Xu, L. Hu, R. Su, W. Liu, X. Fu, Flow characteristics of the air-liquid mixed suction flow in sudden expansion micro-channel, Exp. Therm. Fluid Sci. 130 (2022) 110519.
[16] M.M. Hoque, R. Moreno-Atanasio, E. Doroodchi, J.B. Joshi, G.M. Evans, S. Mitra, Dynamics of a single bubble rising in a quiescent medium, Exp. Therm. Fluid Sci. 132 (2022) 110546.
[17] D. Gao, X. Li, B. Hou, F. Lu, M. Ye, A. Wang, X. Wang, Study of bubble behavior in high-viscosity liquid in a pseudo-2D column using high-speed imaging, Chem. Eng. Sci. 252 (2022) 117532.
[18] C.A. Chen, K.W. Li, T.F. Lin, W.-K. Li, W.-M. Yan, Experimental study on R-410A subcooled flow boiling heat transfer and bubble behavior inside horizontal annuli, Int. Commun. Heat Mass Transfer 124 (2021) 105283.
[19] S. Fan, F. Duan, A review of two-phase submerged boiling in thermal management of electronic cooling, Int. J. Heat Mass Transfer 150 (2020) 119324.
[20] Y. Fang, W. Yang, D. Xu, L. Hu, L. Su, Y. Huang, Experimental investigation on flow boiling characteristics of R1233zd(E) in a parallel mini-channel heat sink for the application in battery thermal management, Int. J. Heat Mass Transfer 178 (2021) 121591.
[21] T. Ren, Z. Zhu, M. Yan, J. Shi, C. Yan, Experimental study on bubble nucleation and departure for subcooled flow boiling in a narrow rectangular channel, Int. J. Heat Mass Transfer 144 (2019) 118670.
[22] A. Bhattad, J. Sarkar, P. Ghosh, Improving the performance of refrigeration systems by using nanofluids: A comprehensive review, Renew. Sustain. Energy Rev. 82 (2018) 3656–3669.
[23] K.-W. Xu, Y. Zhang, D. Liu, A.N. Azman, H.-B. Kim, Slug flow development study in a horizontal pipe using particle image velocimetry, Int. J. Heat Mass Transfer 162 (2020) 120267.
[24] L. Pavlov, S. Cazin, P. Ern, V. Roig, Exploration by Shake-the-Box technique of the 3D perturbation induced by a bubble rising in a thin-gap cell, Exp. Fluids 62 (1) (2021).
[25] Y. Huang, N. Gui, X. Yang, J. Tu, S. Jiang, H. Zhu, Local measurement of bubbly flow in helically coiled tubes using double-sensor conductivity probe, J. Nucl. Sci. Technol. 57 (2020) 689–703.
[26] Y. He, C. Hu, H. Li, X. Hu, D. Tang, Reliable predictions of bubble departure frequency in subcooled flow boiling: A machine learning-based approach, Int. J. Heat Mass Transfer 195 (2022).
[27] S. Haase, S. Marschner, M.M. Ayubi, M. Lange, Gas-liquid flow in small channels: Artificial neural network classifiers for flow regime prediction, Chem. Eng. Process. Process Intensif. 180 (2022).
[28] P. Zhou, R. Huang, S. Huang, Y.u. Zhang, X. Rao, Experimental investigation on active nucleation site density and bubble departure frequency in subcooled flow boiling by using bubble tracking algorithm, Int. J. Heat Mass Transfer 148 (2020) 119081.
[29] A. Kumar, T. Kumaresan, A.B. Pandit, J.B. Joshi, Characterization of flow phenomena induced by ultrasonic horn, Chem. Eng. Sci. 61 (2006) 7410–7420.
[30] H.-Y. Kim, Y.G. Kim, B.H. Kang, Enhancement of natural convection and pool boiling heat transfer via ultrasonic vibration, Int. J. Heat Mass Transfer 47 (2004) 2831–2840.
[31] R. Azadi, D.S. Nobes, Local flow dynamics in the motion of slug bubbles in a flowing mini square channel, Int. J. Heat Mass Transfer 178 (2021) 121588.
[32] S.V.B. Vivekanand, V.R.K. Raju, Modulated wall motion approach for augmenting slug flow heat transfer between two micro-parallel plates, Phys. Fluids 32 (3) (2020) 032001.
[33] M. Takeyama, T. Kunugi, Flow behavior around single nucleate boiling bubble quantitatively grasped by particle tracking visualization, Int. J. Multiphase Flow 129 (2020) 103295.
[34] C. Poncet, S. Ferrouillat, L. Vignal, A. Memponteil, O. Bulliard-Sauret, N. Gondrexon, Enhancement of heat transfer in forced convection by using dual low-high frequency ultrasound, Ultrason. Sonochem. 71 (2021), 105351.
[35] F. Yu, X. Luo, B. He, J. Xiao, W. Wang, J. Zhang, Experimental investigation of flow boiling heat transfer enhancement under ultrasound fields in a minichannel heat sink, Ultrason. Sonochem. 70 (2021), 105342.
[36] X. Luan, Y. Xie, J. He, L. Zhang, C. Li, X. Zhang, Near-duplicate video detection algorithm based on global GSP feature and local ScSIFT Feature fusion, J. Phys.: Conf. Series 960 (2018) 012034.
[37] P.M.D. Comaniciu, Mean shift: a robust approach toward feature space analysis, IEEE Trans. Pattern Anal. Mach. Intell. 24 (2002) 603–619.
[38] X. Cao, B. Qiu, G. Xu, BorderShift: toward optimal MeanShift vector for cluster boundary detection in high-dimensional data, Pattern Anal. Appl. 22 (2018) 1015–1027.
[39] R.L. Mohanty, M.K. Das, A critical review on bubble dynamics parameters influencing boiling heat transfer, Renew. Sustain. Energy Rev. 78 (2017) 466–494.
[40] J. Garcia, A.J. Barker, M. Markl, The Role of Imaging of Flow Patterns by 4D Flow MRI in Aortic Stenosis, JACC Cardiovasc. Imaging 12 (2019) 252–266.
[41] R. Sadeghi, N. Gasner, S. Khodaei, J. Garcia, Z. Keshavarz-Motamed, Impact of mixed valvular disease on coarctation hemodynamics using patient-specific lumped parameter and Lattice Boltzmann modeling, Int. J. Mech. Sci. 217 (2022) 107038.
[42] H. Wang, P. Ge, S. Wu, B. Wang, Y. Wang, X. Kong, Y. Pang, Improvement method of high-temperature digital image correlation measurement accuracy based on image processing, Measurement 190 (2022) 110723.
[43] J. Ye, H. Ji, X. Zhang, Digital image correlation method based on quasi-conformal mapping for large deformation measurement, Opt. Lasers Eng. 153 (2022) 106985.
[44] D.i. Liu, S. Wang, X. Cui, An artificial neural network supported Wiener process based reliability estimation method considering individual difference and measurement error, Reliab. Eng. Syst. Saf. 218 (2022) 108162.
[45] H. Zhou, X. Niu, An image processing algorithm for the measurement of multiphase bubbly flow using predictor-corrector method, Int. J. Multiphase Flow 128 (2020) 103277.
[46] A. Satou, J. Sagawa, HaoMin Sun, Y. Sibamoto, T. Yonomoto, Error in bubble velocity measurement using 4-sensor void probe due to interface deformation, Nucl. Eng. Design 379 (2021) 111234.
[47] L. Yin, L. Jia, P. Guan, D. Liu, Experimental investigation on bubble confinement and elongation in microchannel flow boiling, Exp. Therm. Fluid Sci. 54 (2014) 290–296.
[48] G.K. Sinha, S. Mahimkar, A. Srivastava, Schlieren-based simultaneous mapping of bubble dynamics and temperature gradients in nucleate flow boiling regime: Effect of flow rates and degree of subcooling, Exp. Therm. Fluid Sci. 104 (2019) 238–257.
[49] G.K. Sinha, A. Srivastava, Experiments to compare the dynamics and thermal impact of single vapor bubble subjected to upward and downward flow boiling configurations, Exp. Heat Transfer 33 (2019) 487–509.
[50] B. Agostini, R. Revellin, J.R. Thome, Elongated bubbles in microchannels. Part I: Experimental study and modeling of elongated bubble velocity, Int. J. Multiphase Flow 34 (6) (2008) 590–601.
[51] G.K. Sinha, A. Srivastava, Whole field measurements to quantify the thermal impact of single vapor bubble under nucleate flow boiling regime, Int. J. Heat Mass Transfer 157 (2020) 119932.
[52] B.B. Bayazit, D.K. Hollingsworth, L.C. Witte, Heat transfer enhancement caused by sliding bubbles, J. Heat Transfer-Trans. ASME 125 (2003) 503–509.
[53] B. Donnelly, T.S. O'Donovan, D.B. Murray, Surface heat transfer due to sliding bubble motion, Appl. Therm. Eng. 29 (2009) 1319–1326.
[54] P. Guan, L. Jia, L. Yin, S. Wang, Experimental investigation of bubble behaviors in subcooled flow boiling, J. Therm. Sci. 21 (2012) 184–188.
[55] L. Yin, L. Jia, M. Xu, Experimental investigation on bubble sliding during subcooled flow boiling in microchannel, Exp. Therm Fluid Sci. 68 (2015) 435–441.

[56] J. Zhou, X. Luo, C. Li, L. Liang, G. Wang, B. He, Z.Q. Tian, Flow boiling heat transfer enhancement under ultrasound field in minichannel heat sinks, Ultrason. Sonochem. 78 (2021), 105737.
[57] S.G. Kandlikar, Nucleation characteristics and stability considerations during flow boiling in microchannels, Exp. Therm. Fluid Sci. 30 (2006) 441–447.
[58] W.H. Wu, D.G. Eskin, A. Priyadarshi, T. Subroto, I. Tzanakis, W. Zhai, New insights into the mechanisms of ultrasonic emulsification in the oil-water system and the role of gas bubbles, Ultrason. Sonochem. 73 (2021), 105501.